Elsevier Editorial System(tm) for NeuroImage
Manuscript Draft

Manuscript Number: NIMG-16-1402R2

Title: Tradeoffs in pushing the spatial resolution of fMRI for the 7 T Human Connectome Project

Article Type: SI:Cleaning fMRI time series

Section/Category: fMRI Acquisition/Physics

Corresponding Author: Dr. An Thanh Vu, Ph.D.

Corresponding Author's Institution: University of California Berkeley

First Author: An Thanh Vu, Ph.D.

Order of Authors: An Thanh Vu, Ph.D.; Keith Jamison; Matthew F Glasser; Stephen M Smith; Timothy Coalson; Steen Moeller; Edward J Auerbach; Kamil Ugurbil; Essa Yacoub

Abstract: Whole-brain functional magnetic resonance imaging (fMRI), in conjunction with multiband acceleration, has played an important role in mapping the functional connectivity throughout the entire brain with both high temporal and spatial resolution. Ultrahigh magnetic field strengths (7 T and above) allow functional imaging with even higher functional contrast-to-noise ratios for improved spatial resolution and specificity compared to traditional field strengths (1.5 T and 3 T). High-resolution 7 T fMRI, however, has primarily been constrained to smaller brain regions given the amount of time it takes to acquire the number of slices necessary for high resolution whole brain imaging.

Here we evaluate a range of whole-brain high-resolution resting state fMRI protocols (0.9, 1.25, 1.5, 1.6 and 2 mm isotropic voxels) at 7 T, obtained with both in-plane and slice acceleration parallel imaging techniques to maintain the temporal resolution and brain coverage typically acquired at 3 T. Using the processing pipeline developed by the Human Connectome Project, we demonstrate that high resolution images acquired at 7 T provide increased functional contrast to noise ratios with significantly less partial volume effects and more distinct spatial features, potentially allowing for robust individual subject parcellations and descriptions of fine-scaled patterns, such as visuotopic organization.

Introduction:

Functional magnetic resonance imaging (fMRI) (Bandettini et al., 1992; Kwong et al., 1992; Ogawa et al., 1992) is the most commonly used non-invasive method for studying human brain function. Although the blood oxygen-level dependent (BOLD) signal measured with fMRI is only an indirect measure of neural activity, the two are closely coupled (Logothetis et al., 2001). By pushing the limits of the acquired spatial resolution at high magnetic field strengths and exploiting field and pulse sequence dependent characteristics of the functional mapping signals (e.g., see reviews (Uğurbil et al., 2003; Uğurbil, 2014; Uludağ and Uğurbil, 2015)), recent studies have found that specificity of the BOLD signal to neural activity is sufficient for imaging human brain function down to the columnar (Yacoub et al., 2007, 2008; Cheng et al., 2001; De Martino et al., 2015; Menon et al., 1997; Nasr et al., 2016) and laminar (De Martino et al., 2015; Harel et al., 2006; Muckli et al., 2015; Olman et al., 2012; Polimeni et al., 2010; Zhao et al., 2006; Zimmermann et al., 2011) levels, with some of the studies achieving both columnar and laminar resolution (De Martino et al., 2015; Zimmermann et al., 2011).

Ultrahigh magnetic fields (7 T and above) provide fMRI signals with improved functional contrast-to-noise (fCNR) ratio as well as fidelity to cortical territory of neuronal activity that induces them ((Ugurbil, 2016) and references therein). In order to take full advantage of this high fCNR and spatial fidelity, image acquisition with intrinsically higher spatial resolution is required. Spatial resolution is primarily determined by the volume of the smallest imaging unit (i.e. voxel) and affects the ability of BOLD fMRI data to distinguish activity from distinct functional sub-units such as cortical layers and columns. While the Nyquist sampling criteria (i.e. aliasing) and Rayleigh criteria (i.e. two-point discrimination) are of fundamental importance with regards to mapping the underlying spatial distribution of functional sub-units, equally important is the ability to segregate functional mapping signals of microvascular origin (that would provide high spatial fidelity to the functional sub-units) from non-specific contributions of large draining veins. These confounds, which often manifest as partial volume effects (De Martino et al., 2011; Yacoub et al., 2003), improve with increasing image resolution (i.e. decreasing voxel volume) that is ultimately limited by the signal-to-noise ratio (SNR) and fCNR of the acquired data. In this context, ultrahigh fields provide major advantageous because of significant field dependent gains in SNR (Vaughan et al., 2001; Pohmann et al., 2016), in fCNR associated with the microvasculature (Yacoub et al., 2001, 2003; Ugurbil, 2016), and the decreasing intravascular (relative to extravascular) component of the BOLD signal (Duong et al., 2003; Uludağ et al., 2009). Together, these effects facilitate the segregation of BOLD signals coming from macro and microvasculature sources and, ultimately, the imaging of human brain function at the functional sub-unit level.

Despite the advantages of ultrahigh field strengths, high resolution gradient-echo echo-planar imaging (GE EPI) fMRI with whole brain coverage at 7 T is still challenging both technically and methodologically (Moeller et al., 2010; De Martino et al., 2011). Due to the shorter T2 and T2* values at higher field strengths (Jezzard et al 1996, Debiao Li et al 1998, Wanasapura 1999, Kruger et al 2001, Yacoub et al 2001, and for review see Uludağ et al., 2009), shorter acquisition times (i.e. echo train lengths) are required in order to minimize geometric distortions/blurring, susceptibility induced artifacts, and to maximize fCNR. Segmented EPI acquisitions have been used to reduce echo train lengths (McKinnon, 1993; Feinberg and Oshio, 1994; Wielopolski et al., 1995), however, this results in increased sensitivity to physiological noise and motion (Moeller et al., 2006) as well as increased volume acquisition times (TR). With the advent of multi-channel receiver coils, in-plane parallel imaging (Sodickson and Manning, 1997; Pruessmann et al., 1999; Griswold et al., 2002), and slice acceleration methods (Larkman et al., 2001; Moeller et al., 2010; Setsompop et al., 2012), many of the aforementioned technical limitations at high fields have been significantly mitigated. However, even for modest spatial resolutions, the use of in-plane accelerations is necessary at 7 T (unlike at 3 T) and, as such, plays a significant role in protocol optimizations at this ultrahigh magnetic field strength.

It is in this context, the Human Connectome Project (HCP) (Smith et al., 2013; Uğurbil et al., 2013; Van Essen et al., 2013) investigated tradeoffs in pushing the limits of spatial and temporal resolutions for fMRI applications at high fields with the goal of generating a detailed *in vivo* mapping of functional connectivity in the healthy adult human brain across a large cohort (1200 subjects at 3 T and 180 subjects at 7 T). Early on, the project focused primarily on optimizing slice acceleration and resolution at 3 T for resting state fMRI (rfMRI) and was able to advance from a traditional, unaccelerated resolution of ~3 mm isotropic (27 mm^3, TR=3000 ms) to an accelerated resolution of 2 mm isotropic (8 mm^3 voxel volume) with TR=720ms for whole brain coverage. Impressively, this factor of 3.4 reduction in voxel volume was obtained with little cost to image quality, fCNR, or SNR per unit time (Smith et al., 2013; Xu et al., 2013) and the factor of 4 increase in temporal sampling facilitated novel studies on resting state network dynamics (Smith et al., 2012). Importantly, partial volume effects were also greatly reduced given that the majority of cortex is less than 3 mm thick (Glasser et al., 2013, 2016b).

Here we describe subsequent work by the HCP, taking the initial advancements obtained at 3 T and pushing spatial resolution even further at ultrahigh field strengths (Uğurbil et al., 2013; Vu et al., 2015). We demonstrate that the conventional HCP analysis pipeline designed from 3 T HCP data (Glasser et al., 2013) can be applied to whole-brain, high-resolution rfMRI data acquired at 7 T. To assess the impact of spatial resolution on the resultant detectability of resting state networks throughout the brain, we compare 7 T data acquired at various isotropic spatial resolutions (2 mm, 1.6 mm, 1.5 mm, 1.25 mm, and 0.9 mm) using the 2 mm 3 T HCP rfMRI data as baseline. When analyzing the data at the resolution of the original 2 mm grayordinate space (Glasser et al., 2013), 7 T functional networks show enhanced fCNR, resulting in sharper, stronger, and more well defined spatial detail even at the group level, relative to those acquired with the lower resolution 3 T HCP protocol.

Methods:

Data acquisition:

All data were acquired on a Siemens 7 T Magnetom system, 3 T Trio, or 3 T customized HCP Skyra system using standard 32-channel receive coil arrays. Pilot data for in-depth comparisons of various resolutions and acceleration factors at 7 T was acquired from two non-HCP subjects in five separate scan sessions using the protocols described in Table 1. One of these subjects was scanned in a sixth scan session with what was later to become the final HCP 7 T fMRI protocol. For comparison of the final HCP 3 T and 7 T protocols (rightmost two columns in Table 1), data from an early subset of 24 HCP subjects, scanned at both 3 T and 7 T, were selected for evaluation. For each scan protocol tested, 4 x 15 min resting scans were acquired in which subjects were instructed to rest motionless and awake with their eyes open and fixated on a small fixation cross. HCP 3 T data obtained on the HCP Skyra system was acquired with RL / LR phase encoding directions, with half the runs acquired with RL and the other half with LR phase encoding, to average out susceptibility induced effects (Glasser et al., 2013; Smith et al., 2013); the RL/LR choice enabled a smaller FOV for additional reduction in readout train length, TE, and TR. However, because of the gradient performance differences, the 7 T data utilized AP/PA phase encoding direction, with AP encoding direction for half the time series points and PA for the other half. Spin-echo EPI phase encoding direction reversed pairs were acquired for each resolution condition to estimate and correct for susceptibility-induced EPI distortions (Andersson et al., 2003).

fMRI Protocols	**3 T**	**7 T**	**7 T**	**7 T**	**7 T**	**HCP 3 T**	**HCP 7 T**
Nominal Resolution (mm)	2.00	2.00	1.50	1.25	0.90	2.00	1.60
TR (ms)	774	702	1355	1946	3733	720	1000
TE (ms)	34.2	18.0	18.0	19.4	21.2	33.1	22.2
FOV (mm)	208x208	212x212	210x210	210x210	210x210	208x180	208x208
Partial Fourier	7/8	7/8	7/8	6/8	5/8	Off	7/8
Echo Spacing (ms)	0.69	0.59	0.66	0.74	1.00	0.58	0.64
Echo Train Length (ms)	62.8	27.5	40.6	31.3	50.0	52.2	36.5
Slices	72	75	87	108	150	72	85
Acceleration	MB8	iPAT2 MB5	iPAT3 MB3	iPAT3 MB3	iPAT3 MB3	MB8	iPAT2 MB5

Table 1. 7T fMRI protocols evaluated in the piloting phase. iPAT factor refers to the acceleration factor along the phase encoding direction. Rightmost two columns contain the final HCP protocols, for comparison. HCP 3 T data was acquired on the custom HCP Skyra system of the WU-Minn HCP consortium.

As with the 3 T HCP fMRI protocol, MB acceleration is highly desirable at 7 T, particularly given the increased number of imaging slices required (>128) to cover the whole brain at higher nominal isotropic spatial resolution. However, while longer T_2^* at 3 T permitted the HCP 3 T protocol to forgo in-plane accelerations (benefitting SNR), for the resolutions tested at 7 T, in-plane undersampling (Griswold et al., 1999) was necessary. The need for in-plane acceleration limits the amount of multislice acceleration that can be concurrently achieved, as they both rely on the same coil sensitivity profiles for spatial encoding. With the 32-channel coil used on our 7 T system, in terms of image quality, blurring, and SNR (gained from the shorter attainable TE and the higher magnetic field), an in-plane phase encoding acceleration factor between 2-3 (referred to as integrated-Parallel Acquisition-Techniques or iPAT factor in Siemens terminology) was found to be optimal when simultaneously using a slice acceleration MB factor between 3-5. A 2D (MB x iPAT) total acceleration factor of ~10 (5x2 or 3x3) resulted in optimal TR and SNR per unit time; such high acceleration factors are feasible due to field dependent gains parallel imaging (Wiesinger et al., 2004) and has been previously demonstrated for 7T (e.g. (Moeller et al., 2006, 2010)). To allow the acceleration gains from MB to be fully exploited, phase optimized MB RF sub-pulses were utilized (Wong, 2012) . This optimization results in reduction of peak power requirements as well as mitigation of SAR overestimation errors (Vu et al., 2015), thereby permitting the shortest possible TRs.

The reference scan for the in-plane acceleration is typically acquired using multi-shot EPI, segmented along the phase encoding direction. As mentioned previously, such segmented acquisitions are easily degraded in the presence of motion as well as physiological fluctuations (Moeller et al., 2006). The problem is further compounded when the reference scans become very long (~30-120 sec; e.g., when high resolution is sought or when both in-plane and slice accelerations are used). Previous work has shown that alternative reference scans can reduce motion sensitivity in low resolution (e.g. 3 mm) in-plane accelerated 2D EPI (Griswold et al., 2006; Polimeni et al., 2016; Talagala et al., 2013; Uğurbil et al., 2013). We found similar advantages when using the GRE FLASH reference scan in the context of high-resolution slice and in-plane accelerated 2D GE and SE EPI (Uğurbil et al., 2013; Vu et al., 2015). We employed this reference scan in the final HCP 7 T protocol but not during the pilot study as it was not available at the time.

With B_1^+ (transmit) inhomogeneity increasing with field strength, methods to reduce such inhomogeneity are also important at 7 T for optimal SNR and fCNR. Advanced parallel transmit (pTx) Multiband pulse design techniques hold promise to deal with this B_1^+ inhomogeneity problem in MB based acquisitions (Wu et al., 2014, 2016; Guérin et al., 2015; Poser et al., 2014). However, this technology is still in development and at the time was not sufficiently mature in implementation for routine and repeated use as demanded by the HCP. We therefore opted for an alternative, passive B_1^+ shimming approach, which has been shown to locally improve B_1^+ transmit efficiency, with practically no detrimental impact on SAR or image quality (Haines et al., 2010; Teeuwisse et al., 2012; Vu et al., 2015). Our approach involved careful placement of 5 mm thick, high permittivity dielectric pads under the neck and on both sides of the head to improve the generally poor B_1^+ in the cerebellum and temporal lobes by upwards of a factor of two in flip angle. The pads consisted of a 3:1 mass ratio suspension of calcium titanate powder in water, chosen for its high relative permittivity ($\varepsilon_r \approx 110$), chemical inertness and non-toxic properties.

Data Processing:

All data were pre-processed using the HCP pipeline (Glasser et al., 2013) . The HCP pre-processing pipeline is very conservative with regards to temporal frequency filtering. Minimal highpass filtering is applied (using the −bptf option in FSL's fslmaths tool), with a “cutoff” of 2000s (i.e., FWHM = 2355 s; note that data length is ~900 s/run). The effect of this filter is therefore similar to linear detrending of the data. No lowpass filtering was applied.

ICA-based artifact removal was used to remove non-neural spatiotemporal components from each 15-minute run of fMRI data. The removal of artifacts was carried out for each run separately. Once ICA identified a number of artifactual components, the data were “cleaned” by regressing out these components from the data. The overall approach is referred to as FIX (FMRIB's ICA-based X-noisifier); the FIX approach and initial results of classification accuracy are described in detail in (Salimi-Khorshidi et al., 2014), and the effects of the ICA + FIX cleanup (and optimal methods to remove the bad components from the data) are evaluated in detail in (Griffanti et al., 2014).

ICA was run on the volumetric data using MELODIC (Beckmann and Smith, 2004) with automatic dimensionality estimation (MELODIC estimates how many components the given quality and quantity of data will support being separated from each other); with dimensionality limited to a maximum of 250 for computational efficiency. These components were fed into FIX, which classifies components into "good" vs. "bad" for the 3 T data. The classified components were then manually checked for accuracy. The 7 T data were classified manually into the "good" and "bad" components as FIX was not trained on high-resolution 7 T data at that time, and a FIX classification training does not necessarily generalize across different spatial and temporal resolutions. A FIX classifier has since been trained on 1.6mm 7 T HCP data in preparation for the 7 T HCP data release (and has been demonstrated to have an accuracy of 98.4% in cross subject validation testing). The set of artifactual processes was then removed from the grayordinates version of the data by regressing out the bad components' timeseries. For both volume and surface cleanup, the cleanup was done in a "non-aggressive" manner — both the good and bad component timeseries were regressed into the data, and then the resulting bad spatial (regression parameter) maps were multiplied by the associated timeseries and subtracted from the original dataset. Thus, only the unique variance associated with the bad components was removed from the data. For additional details regarding data preprocessing and resting state analysis see Glasser et al., 2013 and Smith et al., 2013, respectively.

Effective gains in resolution (e.g., reduction in partial volume effects) between the different pilot protocols were quantified using a "cross-sulcal correlation ratio metric" at each vertex in grayordinate space. This metric takes the ratio of two temporal correlation-based measures. The first one being "cross sulcal": between a given vertex and vertices close in 3D Euclidian distance but far in 2D geodesic distance (i.e. along the cortical surface). The second one being "within sulcus": the average of correlations between the given vertex and a set of vertices close in both 2D and 3D distance. Thus larger values indicate broader point spread functions (PSF), more partial volume effects and lower effective resolution. More specifically, for each individual vertex, the set of vertices within 4 mm 3D Euclidean distance, and where the Euclidean distance to the vertex is less than a third of the 2D geodesic distance to the same vertex (Glasser et al., 2013), was found (i.e., if a vertex is 2mm in Euclidean distance from the chosen vertex, and its geodesic distance from the chosen vertex is 9mm, it is included, while if its geodesic distance was 5mm, it would be excluded). From this set, the vertex with the smallest 3D Euclidean distance was chosen as the "across sulcal/gyral bank" vertex, and its correlation to the central vertex was computed. Next, the set of vertices with geodesic distances from the center vertex between 4 mm and 6 mm were found (to approximate the correlation to similar functioning gray matter, while preventing artificial bias caused by mixing signal from the center vertex into nearby vertices), and their correlations to the center vertex were computed, and averaged. The output value for the vertex is the correlation to the "across sulcal/gyral bank" vertex divided by the mean of the correlations to the nearby vertices. A summary value for each resolution condition is reported as the median of this “correlation ratio metric” across all cortical vertices in a given subject’s brain.

Results and Discussion:

Figure 1 shows representative, distortion corrected GE EPI axial slices from a single subject from the pilot study (i.e. acquired with slice and in-plane accelerations using segmented EPI reference scans, as opposed to the FLASH reference scans used in the final 7T HCP protocol). Across all resolutions tested, the 7 T datasets yielded noticeably stronger T2* gray-white matter contrast. Delineation of finer structures is seen as voxel sizes are reduced down to the 0.9 mm resolution. Note the striping artifact in the brain stem and cerebellum regions of the 1.5 mm and higher data (red arrows in Figure 1B). These are due to the enhanced motion sensitivity in the iPAT3 segmented EPI reference scans, which, based on such data, were replaced with FLASH reference scans in the final HCP protocol to eliminate this artifact. The 7 T 1.6 mm protocol is more robust to motion artifacts given its reduced in-plane segmentation (iPAT 2) and shorter overall reference scan.

Figure 2 shows a representative subject’s seed based connectivity map in volumetric MNI space with a seed voxel placed in primary visual cortex for both the 3 T and 7 T HCP protocols. Impressively, even with the substantially smaller voxel volume, the 7 T data results in similar if not stronger correlation values than the 3 T data. Furthermore, benefiting from the reduced partial voluming, the 7 T data reveals broader connectivity maps, which extends into sulcal regions where the cortex is relatively thin. Note: to control for the different number of timepoints, only the top 50 PCA components were used when calculating the correlation values.

Figure 3 shows the cross-sulcal to within-sulcal correlation ratio as a function of field strength and resolution. The box plots show the mean (red lines), 25 and 75 percentiles (blue boxes), as well as maximum and minimum data points ("whiskers"), across the four resting state scans per resolution for pilot subjects 1 and 2. As expected, the metric is very similar for both 3 T and 7 T with 2 mm isotropic resolution datasets, and decreases significantly in going from 2 mm to 1.5 mm isotropic resolution ($p < 0.05$, T(6) for both subjects). Blurring in the phase encoding direction associated with increased partial Fourier and echo train lengths required for higher resolution acquisitions are also reflected in these results. Thus, the effective resolution at higher acquired "nominal" resolutions is likely not better than what was achieved with 1.5 mm isotropic nominal resolution. In addition, post-processing steps may also have contributed to this since enhanced anatomical detail is apparent in the raw EPI images themselves (Figure 1) when the resolution is improved beyond 1.5 mm isotropic. In any case, the 1.5 mm limit may be imposed by the PSF of the gradient-echo T2* contrast mechanism (Engel et al., 1997; Parkes et al., 2005; Shmuel et al., 2007) which suggest that improvements beyond 1.5 mm may not be significant, if they exist at all, due to the macrovascular contributions. Nevertheless, Figure 3C shows that a significant gain in resolution and reduction in partial volume effects in the final 7 T HCP protocol versus the 3 T HCP protocol was achieved (averaged across 24 HCP subjects, $p < 10^{-10}$, T(24)).

The results of the cross-sulcal/within-sulcal correlation analysis are not in contradiction with high spatial and functional resolution studies conducted at 7 Tesla pursuing columnar and laminar resolution functional mapping. Columnar and laminar resolution efforts use strategies to suppress the macrovascular contributions to functional maps which would show correlated signal-fluctuations over large cortical distances, estimated to be as much as 4 mm (e.g. see (Ugurbil, 2016) and references therein). Such strategies include the use of spin-echo based functional contrast mechanisms, which favors the microvascular effects that provide improved functional fidelity (Yacoub et al., 2007, 2008), or spatially eliminating superficial layers of the cortex from the analysis so as to avoid regions impacted by the large veins on the pial surface (Polimeni et al., 2010), or selectively detecting the voxels that contain non-specific functional information, presumably due to the macrovascular constribution, and eliminatig them from the analysis (Muckli et al., 2015). Columnar and/or laminar type studies also try to minimize the image resolition degredation (i.e. blurring) that comes from EPI k-space trajectory by acquiring highly restricted field-of-view data imposed by inner volume selection (e.g. (De Martino et al., 2015; Zimmermann et al., 2011)) and/or the use higher accelerations for in-plane parallel imaging (Moeller et al., 2010), and/or utilizing segmented acquisitions (albeit at the expense of some degredation in fCNR) together with field-of-view reduction along the phase encode direction (Yacoub et al., 2007, 2008). It is also important to note that, provided that the Nyquist sampling criteria are met, even with a larger PSF, fine-grained functional organizations such as columns and lamina are still theoretically detectable albeit with a reduced fCNR (Yacoub et al., 2008; Muckli et al., 2015).

Figure 4 displays the number of resting state ICA signal components as a function of field strength and resolution for pilot subjects 1 and 2. The number of resting state signal components supported by the data increases for the same spatial resolution in going from 3t to 7T. However, because going to higher resolutions decreases SNR (due to smaller voxel volumes) and the temporal degrees of freedom per unit time (due to longer TRs), going to higher spatial resolution comes at the cost of supporting fewer resting state components classified as signal found by the MELODIC algorithm. This cost can be mitigated by minimizing the reliance on iPAT from a factor of 3 down to a factor of 2 and increasing the MB factor. While retaining optimal TE and echo train blurring, the iPAT 3 MB 3 1.5 mm protocol was optimized to an iPAT 2, MB 5, 1.6 mm protocol (the final 7 T HCP protocol). By doing so, SNR is increased due to fuller k-space sampling per TR as well as reductions in motion sensitivity due to the reduction in number of segments in the segmented EPI reference scan. Furthermore, reducing reliance on iPAT allows a higher MB factor and thus further reduction in the TR, translating to larger number of detectable signal components. Figure 5 shows the resting state component composition of the 3 T versus the final 7 T HCP protocol (averaged across 24 HCP subjects). The total number of ICA components as well as the number of BOLD signal ICA components detected were greater for the 7 T than the 3 T ($p < 0.05$, T(23)), while the number of noise ICA components also tended to be greater for the 7 T than the 3 T.

Figure 6 illustrates the resting state variance breakdown for both the 3 T and 7 T datasets, again on average across the same 24 HCP subjects shown in Figure 5. The unstructured noise divided by original, pre-FIX variance was significantly higher in the 3 T data than the 7 T data ($p < 0.05$, T(23)). Here, unstructured noise is defined as the residual variance remaining not contributed by the ICA components classified as either "noise" or "signal" and provides an estimate of the relative amount of thermal noise in the data. A metric of BOLD SNR calculated as BOLD variance divided by original variance (where BOLD variance is the variance contributed by the ICA components classified as "signal") shows that the 7 T has twice the BOLD SNR as the 3 T data ($p < 0.05$, T(23)). We also calculated fCNR defined as the square root of the BOLD variance divided by the square root of the unstructured noise variance and found this too was twice as great at 7 T relative to 3 T ($p < 0.05$, T(23)), although the difference is slightly reduced when the 28% difference in number of timepoints sampled between the 7 T and 3 T HCP protocols are accounted for (red dashed line).

Figure 7 shows the resting state fCNR for both 7 T divided by the 3 T fCNR, averaged across 24 HCP subjects. The results are displayed in CIFTI grayordinate space and show, on average, a 2:1 advantage of the 7 T HCP rfMRI data across the brain. Note that for fair comparison here, both 3 T and 7 T datasets are processed and displayed in 2 mm grayordinate space. Processing the 7 T data in 1.6 mm grayordinate space (which have been included in the latest HCP public release: www.humanconnectome.org/documentation/S900) or in the native subject space would likely result in additional spatial detail but a corresponding reduction in SNR (by the square-root of the volume reduced). Figure 8 shows how the advantage in 7 T fCNR manifests in terms of dense Connectome connectivity (e.g. correlation coefficient) for an exemplary seed placed in occipital parietal cortex, while Figure 9 shows the advantage in reducing partial volume effects at 7 T for an exemplary seed placed in subcortical nucleus, pulvinar (red arrow). Figure 10 shows how the reductions in partial volume effects and increases in SNR, fCNR and connectivity measured in the 7 T HCP protocol manifests in sharper, stronger, and more well defined dense Connectome connectivity gradients. These improvements in fCNR will be key to providing robust individual subject parcellations and descriptions of fine-scaled patterns, such as visuotopic organization (Glasser et al., 2016a).

Conclusion:

Ultrahigh fields offer improved sensitivity and functional specificity for fMRI applications, facilitating the acquisition of higher resolution images and allowing for a better understanding of intrinsic properties of functional networks. By taking the initial advancements obtained at 3 T in the HCP and pushing spatial resolution even further at ultrahigh field strengths, we demonstrate that high-resolution imaging at the minimum cortical thickness of 1.6mm can be extended to the entire brain with a temporal resolution of 1 second or better. 7 T functional resting state networks showed enhanced fCNR and reduced partial volume effects even at the group level, relative to those acquired with the lower resolution 3 T HCP protocol. Our results suggest that the increased functional contrast to noise ratio at 7 T allows for studying resting state networks using voxel volumes half the size as the 3 T HCP protocol (and 37 times smaller than what is conventionally used at 3 T) with more distinct spatial features, potentially allowing for robust individual subject parcellations and descriptions of fine-scaled patterns, such as visuotopic organization. The improved resolution of the 7 T protocol should also be useful in future investigations of columnar/laminar organizations across cortex.

Figure Captions:

Figure 1. Representative GE EPI cross sections from a single subject. A) Axial slices. Top row: 3 T 2 mm isotropic (left), 7 T 1.6 mm isotropic (middle) and 7 T 1.25 mm isotropic (right). Bottom row: 7 T 2 mm isotropic (left), 7 T 1.5 mm isotropic (middle), 7 T 0.9 mm isotropic (right). B) Sagittal slices. Formatting same as A. Note the striping artifact in the brain stem and cerebellum regions of the 1.5 mm and higher data (red arrow). These are indicative of the enhanced motion sensitivity in the iPAT3 reference scans.

Figure 2. Representative seed based connectivity map from a single subject for both the 3 T and 7 T HCP protocols. The seed voxel is placed in primary visual cortex (denoted by the crosshairs). The 7 T data results in similar if not stronger correlation values than the 3 T data, even though the voxel volume is roughly half that of the 3T data. Benefiting from the reduced partial

voluming, the 7 T data reveals broader connectivity maps, which extends into sulcal regions where the cortex is relatively thin. Note: to control for the different number of timepoints, only the top 50 PCA components were used when calculating the correlation values for both 3 T and 7 T.

Figure 3. Cross-sulcal to within-sulcal correlation ratio as a function of field strength and resolution. A) Box plots calculated across the four resting state scans per resolution for pilot subject 1. As expected, the metric decreases from 2 mm to 1.5 mm. Improvements beyond 1.5 mm may in part be limited due to blurring in the phase encoding direction associated with increased PF and echo train lengths required for higher resolution acquisitions. B) Same as A, but for pilot subject 2. C) Comparison of correlation ratio metric between 3 T and 7 T HCP protocols averaged across 24 HCP subjects. Error bars are STDEV across subjects.

Figure 4. Number of resting state signal components as a function of field strength and resolution. Reducing the iPAT factor to 2, was most efficient in terms of TR and SNR per unit time which translated to larger number of detectable signal components. While retaining optimal TE and echo train blurring a resolution of 1.6 mm was attainable.

Figure 5. Resting state component composition: 3 T vs 7 T, on average across 24 subjects. Left) Total number of ICA components (7 T > 3 T; $p < 0.05$). Middle) Number of noise ICA components. Right) Number of BOLD signal ICA components (7 T > 3 T; $p < 0.05$). Errorbars are STDEV across subjects.

Figure 6. Resting state variance breakdown: 3 T vs 7 T, on average across 24 subjects. Left) Unstructured Noise divided by original variance; where unstructured noise is the residual variance remaining not contributed by the ICA components classified as either “noise” or “signal” (7 T < 3 T; $p < 0.05$). Middle) BOLD variance divided by original variance; where BOLD variance is the variance contributed by the ICA components classified as “signal” (7 T > 3 T; $p < 0.05$). Right) fCNR as defined as square root of the BOLD variance divided by unstructured noise variance (7 T > 3 T; $p < 0.05$). Dashed red line indicated fCNR after compensating for difference in number of timepoints sampled in the 7 T and 3 T HCP protocols. Errorbars are STDEV across subjects.

Figure 7. Resting state fCNR: 7 T vs 3 T, on average across 24 subjects.
The results are displayed in CIFTI grayordinate space and show the advantage of the 7 T protocol across the brain.

Figure 8. Exemplary dense Connectome for a seed placed in posterior parietal cortex. The 7 T data shows enhanced connectivity / correlation throughout the brain.

Figure 9. Exemplary dense Connectome for a seed placed in the subcortical nucleus, pulvinar (red arrow). Due to the improvement in partial voluming, the 7 T data is able to show connectivity / correlation throughout the brain while the 3T data is not.

Figure 10. Dense Connectome connectivity gradients. The 7 T data show stronger, more well defined gradients.

References:

Andersson, J.L.R., Skare, S., Ashburner, J., 2003. How to correct susceptibility distortions in spin-echo echo-planar images: application to diffusion tensor imaging. NeuroImage 20, 870–888. doi:10.1016/S1053-8119(03)00336-7

Bandettini, P.A., Wong, E.C., Hinks, R.S., Tikofsky, R.S., Hyde, J.S., 1992. Time course EPI of human brain function during task activation. Magn. Reson. Med. 25, 390–397. doi:10.1002/mrm.1910250220

Beckmann, C.F., Smith, S.M., 2004. Probabilistic independent component analysis for functional magnetic resonance imaging. IEEE Trans. Med. Imaging 23, 137–152. doi:10.1109/TMI.2003.822821

Cheng, K., Waggoner, R.A., Tanaka, K., 2001. Human Ocular Dominance Columns as Revealed by High-Field Functional Magnetic Resonance Imaging. Neuron 32, 359–374. doi:10.1016/S0896-6273(01)00477-9

De Martino, F., Esposito, F., van de Moortele, P.-F., Harel, N., Formisano, E., Goebel, R., Ugurbil, K., Yacoub, E., 2011. Whole brain high-resolution functional imaging at ultra high magnetic fields: An application to the analysis of resting state networks. NeuroImage, Special Issue: Educational Neuroscience 57, 1031–1044. doi:10.1016/j.neuroimage.2011.05.008

De Martino, F., Moerel, M., Ugurbil, K., Goebel, R., Yacoub, E., Formisano, E., 2015. Frequency preference and attention effects across cortical depths in the human primary auditory cortex. Proc. Natl. Acad. Sci. 112, 16036–16041. doi:10.1073/pnas.1507552112

Duong, T.Q., Yacoub, E., Adriany, G., Hu, X., Uğurbil, K., Kim, S.-G., 2003. Microvascular BOLD contribution at 4 and 7 T in the human brain: Gradient-echo and spin-echo fMRI with suppression of blood effects. Magn. Reson. Med. 49, 1019–1027. doi:10.1002/mrm.10472

Engel, S.A., Glover, G.H., Wandell, B.A., 1997. Retinotopic organization in human visual cortex and the spatial precision of functional MRI. Cereb. Cortex 7, 181–192. doi:10.1093/cercor/7.2.181

Feinberg, D.A., Oshio, K., 1994. Phase errors in multi-shot echo planar imaging. Magn. Reson. Med. 32, 535–539. doi:10.1002/mrm.1910320418

Glasser, M.F., Coalson, T.S., Robinson, E.C., Hacker, C.D., Harwell, J., Yacoub, E., Ugurbil, K., Andersson, J., Beckmann, C.F., Jenkinson, M., Smith, S.M., Van Essen, D.C., 2016. A multi-modal parcellation of human cerebral cortex. Nature advance online publication. doi:10.1038/nature18933

Glasser, M.F., Smith, S.M., Marcus D.S., Andersson J., Auerbach E.J., Coalson, T.S., Harms, M.P., Jenkinson M., Moeller S., Robinson E.C., Sotiropoulos S.N., Xu J., Yacoub E., Ugurbil K., Van Essen D.C., 2016. The Human Connectome Project's neuroimaging approach. Nature Neuroscience 19, 1175-1187. doi:10.1038/nn.4361

Glasser, M.F., Sotiropoulos, S.N., Wilson, J.A., Coalson, T.S., Fischl, B., Andersson, J.L., Xu, J., Jbabdi, S., Webster, M., Polimeni, J.R., Van Essen, D.C., Jenkinson, M., 2013. The minimal preprocessing pipelines for the Human Connectome Project. NeuroImage 80, 105–124. doi:10.1016/j.neuroimage.2013.04.127

Griffanti, L., Salimi-Khorshidi, G., Beckmann, C.F., Auerbach, E.J., Douaud, G., Sexton, C.E., Zsoldos, E., Ebmeier, K.P., Filippini, N., Mackay, C.E., Moeller, S., Xu, J., Yacoub, E., Baselli, G., Ugurbil, K., Miller, K.L., Smith, S.M., 2014. ICA-based artefact removal and accelerated fMRI acquisition for improved resting state network imaging. NeuroImage 95, 232–247. doi:10.1016/j.neuroimage.2014.03.034

Griswold, M. a., Jakob, P. m., Chen, Q., Goldfarb, J. w., Manning, W. j., Edelman, R. r., Sodickson, D. k., 1999. Resolution enhancement in single-shot imaging using simultaneous acquisition of spatial harmonics (SMASH). Magn. Reson. Med. 41, 1236–1245. doi:10.1002/(SICI)1522-2594(199906)41:6<1236::AID-MRM21>3.0.CO;2-T

Griswold, M.A., Breuer, F., Blaimer, M., Kannengiesser, S., Heidemann, R.M., Mueller, M., Nittka, M., Jellus, V., Kiefer, B., Jakob, P.M., 2006. Autocalibrated coil sensitivity estimation for parallel imaging. NMR Biomed. 19, 316–324. doi:10.1002/nbm.1048

Griswold, M.A., Jakob, P.M., Heidemann, R.M., Nittka, M., Jellus, V., Wang, J., Kiefer, B., Haase, A., 2002. Generalized autocalibrating partially parallel acquisitions (GRAPPA). Magn. Reson. Med. 47, 1202–1210. doi:10.1002/mrm.10171

Guérin, B., Setsompop, K., Ye, H., Poser, B.A., Stenger, A.V., Wald, L.L., 2015. Design of parallel transmission pulses for simultaneous multislice with explicit control for peak power and local specific absorption rate. Magn. Reson. Med. 73, 1946–1953. doi:10.1002/mrm.25325

Haines, K., Smith, N.B., Webb, A.G., 2010. New high dielectric constant materials for tailoring the B1+ distribution at high magnetic fields. J. Magn. Reson. 203, 323–327. doi:10.1016/j.jmr.2010.01.003

Harel, N., Lin, J., Moeller, S., Ugurbil, K., Yacoub, E., 2006. Combined imaging–histological study of cortical laminar specificity of fMRI signals. NeuroImage 29, 879–887. doi:10.1016/j.neuroimage.2005.08.016

Jezzard, P., Duewell, S. and Balaban, R. S., 1996. MR relaxation times in human brain: Measurement at 4 T. Radiology. 199, 773-779.

Kruger, G., Kastrup, A. and Glover, G. H., 2001. Neuroimaging at 1.5 T and 3.0 T: Comparison of oxygenation-sensitive magnetic resonance imaging. Magnetic Resonance in Medicine. 45, 595-604.

Kwong, K.K., Belliveau, J.W., Chesler, D.A., Goldberg, I.E., Weisskoff, R.M., Poncelet, B.P., Kennedy, D.N., Hoppel, B.E., Cohen, M.S., Turner, R., 1992. Dynamic magnetic resonance imaging of human brain activity during primary sensory stimulation. Proc. Natl. Acad. Sci. 89, 5675–5679.

Larkman, D.J., Hajnal, J.V., Herlihy, A.H., Coutts, G.A., Young, I.R., Ehnholm, G., 2001. Use of multicoil arrays for separation of signal from multiple slices simultaneously excited. J. Magn. Reson. Imaging 13, 313–317. doi:10.1002/1522-2586(200102)13:2<313::AID-JMRI1045>3.0.CO;2-W

Li, D. B., Wang, Y. and Waight, D. J., 1998. Blood oxygen saturation assessment in vivo using T-2* estimation. Magnetic Resonance in Medicine. 39, 685-690.

Logothetis, N.K., Pauls, J., Augath, M., Trinath, T., Oeltermann, A., 2001. Neurophysiological investigation of the basis of the fMRI signal. Nature 412, 150–157. doi:10.1038/35084005

McKinnon, G.C., 1993. Ultrafast interleaved gradient-echo-planar imaging on a standard scanner. Magn. Reson. Med. 30, 609–616. doi:10.1002/mrm.1910300512

Menon, R.S., Ogawa, S., Strupp, J.P., 1997. Ocular Dominance in Human V1 Demonstrated by Functional Magnetic Resonance Imaging. J Neurophysiol 77, 2780–2787.

Moeller, S., Van de Moortele, P.-F., Goerke, U., Adriany, G., Uğurbil, K., 2006. Application of parallel imaging to fMRI at 7 Tesla utilizing a high 1D reduction factor. Magn. Reson. Med. 56, 118–129. doi:10.1002/mrm.20934

Moeller, S., Yacoub, E., Olman, C.A., Auerbach, E., Strupp, J., Harel, N., Uğurbil, K., 2010. Multiband multislice GE-EPI at 7 tesla, with 16-fold acceleration using partial parallel imaging with application to high spatial and temporal whole-brain fMRI. Magn. Reson. Med. 63, 1144–1153. doi:10.1002/mrm.22361

Muckli, L., De Martino, F., Vizioli, L., Petro, L.S., Smith, F.W., Ugurbil, K., Goebel, R., Yacoub, E., 2015. Contextual Feedback to Superficial Layers of V1. Curr. Biol. 25, 2690–2695. doi:10.1016/j.cub.2015.08.057

Nasr, S., Polimeni, J.R., Tootell, R.B.H., 2016. Interdigitated Color- and Disparity-Selective Columns within Human Visual Cortical Areas V2 and V3. J. Neurosci. 36, 1841–1857. doi:10.1523/JNEUROSCI.3518-15.2016

Ogawa, S., Tank, D.W., Menon, R., Ellermann, J.M., Kim, S.G., Merkle, H., Ugurbil, K., 1992. Intrinsic signal changes accompanying sensory stimulation: functional brain mapping with magnetic resonance imaging. Proc. Natl. Acad. Sci. U. S. A. 89, 5951–5955. doi:VL - 89

Olman, C.A., Harel, N., Feinberg, D.A., He, S., Zhang, P., Ugurbil, K., Yacoub, E., 2012. Layer-Specific fMRI Reflects Different Neuronal Computations at Different Depths in Human V1. PLOS ONE 7, e32536. doi:10.1371/journal.pone.0032536

Parkes, L.M., Schwarzbach, J.V., Bouts, A.A., Deckers, R. h R., Pullens, P., Kerskens, C.M., Norris, D.G., 2005. Quantifying the spatial resolution of the gradient echo and spin echo BOLD response at 3 Tesla. Magn. Reson. Med. 54, 1465–1472. doi:10.1002/mrm.20712

Pohmann, R., Speck, O., Scheffler, K., 2016. Signal-to-noise ratio and MR tissue parameters in human brain imaging at 3, 7, and 9.4 tesla using current receive coil arrays. Magn. Reson. Med. 75, 801–809. doi:10.1002/mrm.25677

Polimeni, J.R., Bhat, H., Witzel, T., Benner, T., Feiweier, T., Inati, S.J., Renvall, V., Heberlein, K., Wald, L.L., 2016. Reducing sensitivity losses due to respiration and motion in accelerated echo planar imaging by reordering the autocalibration data acquisition. Magn. Reson. Med. 75, 665–679. doi:10.1002/mrm.25628

Polimeni, J.R., Fischl, B., Greve, D.N., Wald, L.L., 2010. Laminar analysis of 7 T BOLD using an imposed spatial activation pattern in human V1. NeuroImage 52, 1334–1346. doi:10.1016/j.neuroimage.2010.05.005

Poser, B.A., Anderson, R.J., Guérin, B., Setsompop, K., Deng, W., Mareyam, A., Serano, P., Wald, L.L., Stenger, V.A., 2014. Simultaneous multislice excitation by parallel transmission. Magn. Reson. Med. 71, 1416–1427. doi:10.1002/mrm.24791

Pruessmann, K.P., Weiger, M., Scheidegger, M.B., Boesiger, P., 1999. SENSE: Sensitivity encoding for fast MRI. Magn. Reson. Med. 42, 952–962. doi:10.1002/(SICI)1522-2594(199911)42:5<952::AID-MRM16>3.0.CO;2-S

Salimi-Khorshidi, G., Douaud, G., Beckmann, C.F., Glasser, M.F., Griffanti, L., Smith, S.M., 2014. Automatic denoising of functional MRI data: Combining independent component analysis and hierarchical fusion of classifiers. NeuroImage 90, 449–468. doi:10.1016/j.neuroimage.2013.11.046

Setsompop, K., Gagoski, B.A., Polimeni, J.R., Witzel, T., Wedeen, V.J., Wald, L.L., 2012. Blipped-controlled aliasing in parallel imaging for simultaneous multislice echo planar imaging with reduced g-factor penalty. Magn. Reson. Med. 67, 1210–1224. doi:10.1002/mrm.23097

Shmuel, A., Yacoub, E., Chaimow, D., Logothetis, N.K., Ugurbil, K., 2007. Spatio-temporal point-spread function of fMRI signal in human gray matter at 7 Tesla. NeuroImage 35, 539–552. doi:10.1016/j.neuroimage.2006.12.030

Smith, S.M., Beckmann, C.F., Andersson, J., Auerbach, E.J., Bijsterbosch, J., Douaud, G., Duff, E., Feinberg, D.A., Griffanti, L., Harms, M.P., Kelly, M., Laumann, T., Miller, K.L., Moeller, S., Petersen, S., Power, J., Salimi-Khorshidi, G., Snyder, A.Z., Vu, A.T., Woolrich, M.W., Xu, J., Yacoub, E., Uğurbil, K., Van Essen, D.C., Glasser, M.F., 2013. Resting-state fMRI in the Human Connectome Project. NeuroImage, Mapping the Connectome 80, 144–168. doi:10.1016/j.neuroimage.2013.05.039

Smith, S.M., Miller, K.L., Moeller, S., Xu, J., Auerbach, E.J., Woolrich, M.W., Beckmann, C.F., Jenkinson, M., Andersson, J., Glasser, M.F., Van Essen, D.C., Feinberg, D.A., Yacoub, E.S., Ugurbil, K., 2012. Temporally-independent functional modes of spontaneous brain activity. Proc. Natl. Acad. Sci. 109, 3131–3136. doi:10.1073/pnas.1121329109

Sodickson, D.K., Manning, W.J., 1997. Simultaneous acquisition of spatial harmonics (SMASH): Fast imaging with radiofrequency coil arrays. Magn. Reson. Med. 38, 591–603. doi:10.1002/mrm.1910380414

Talagala, S., Sarlls, J., Inati, S., 2013. Improved temporal SNR of accelerated EPI using a FLASH based GRAPPA reference scan. Presented at the Proceedings of the 21st Annual Meeting of ISMRM, Salt Lake City, Utah, USA.

Teeuwisse, W.M., Brink, W.M., Haines, K.N., Webb, A.G., 2012. Simulations of high permittivity materials for 7 T neuroimaging and evaluation of a new barium titanate-based dielectric. Magn. Reson. Med. 67, 912–918. doi:10.1002/mrm.24176

Ugurbil, K., 2016. What is feasible with imaging human brain function and connectivity using functional magnetic resonance imaging. Phil Trans R Soc B 371, 20150361. doi:10.1098/rstb.2015.0361

Uğurbil, K., 2014. Magnetic Resonance Imaging at Ultrahigh Fields. IEEE Trans. Biomed. Eng. 61, 1364–1379. doi:10.1109/TBME.2014.2313619

Uğurbil, K., Toth, L., Kim, D.-S., 2003. How accurate is magnetic resonance imaging of brain function? Trends Neurosci. 26, 108–114. doi:10.1016/S0166-2236(02)00039-5

Uğurbil, K., Xu, J., Auerbach, E.J., Moeller, S., Vu, A.T., Duarte-Carvajalino, J.M., Lenglet, C., Wu, X., Schmitter, S., Van de Moortele, P.F., Strupp, J., Sapiro, G., De Martino, F., Wang, D., Harel, N., Garwood, M., Chen, L., Feinberg, D.A., Smith, S.M., Miller, K.L., Sotiropoulos, S.N., Jbabdi, S., Andersson, J.L.R., Behrens, T.E.J., Glasser, M.F., Van Essen, D.C., Yacoub, E., 2013. Pushing spatial and temporal resolution for functional and diffusion MRI in the Human Connectome Project. NeuroImage 80, 80–104. doi:10.1016/j.neuroimage.2013.05.012

Uludağ, K., Müller-Bierl, B., Uğurbil, K., 2009. An integrative model for neuronal activity-induced signal changes for gradient and spin echo functional imaging. NeuroImage 48, 150–165. doi:10.1016/j.neuroimage.2009.05.051

Uludağ, K., Uğurbil, K., 2015. Physiology and Physics of the fMRI Signal, in: Uludag, K., Ugurbil, K., Berliner, L. (Eds.), fMRI: From Nuclear Spins to Brain Functions, Biological Magnetic Resonance. Springer US, pp. 163–213.

Van Essen, D.C., Smith, S.M., Barch, D.M., Behrens, T.E.J., Yacoub, E., Ugurbil, K., 2013. The WU-Minn Human Connectome Project: An overview. NeuroImage, Mapping the Connectome 80, 62–79. doi:10.1016/j.neuroimage.2013.05.041

Vaughan, J. t., Garwood, M., Collins, C. m., Liu, W., DelaBarre, L., Adriany, G., Andersen, P., Merkle, H., Goebel, R., Smith, M. b., Ugurbil, K., 2001. 7T vs. 4T: RF power, homogeneity, and signal-to-noise comparison in head images. Magn. Reson. Med. 46, 24–30. doi:10.1002/mrm.1156

Vu, A.T., Auerbach, E., Lenglet, C., Moeller, S., Sotiropoulos, S.N., Jbabdi, S., Andersson, J., Yacoub, E., Ugurbil, K., 2015. High resolution whole brain diffusion imaging at 7 T for the Human Connectome Project. NeuroImage 122, 318–331. doi:10.1016/j.neuroimage.2015.08.004

Wansapura, J. P., Holland, S. K., Dunn, R. S. and Ball, W. S., 1999. NMR relaxation times in the human brain at 3.0 tesla. Journal of Magnetic Resonance Imaging. 9, 531-538.

Wielopolski, P.A., Manning, W.J., Edelman, R.R., 1995. Single breath-hold volumetric imaging of the heart using magnetization-prepared 3-dimensional segmented echo planar imaging. J. Magn. Reson. Imaging 5, 403–409. doi:10.1002/jmri.1880050406

Wiesinger, F., Van de Moortele, P.-F., Adriany, G., De Zanche, N., Ugurbil, K., Pruessmann, K.P., 2004. Parallel imaging performance as a function of field strength—An experimental investigation using electrodynamic scaling. Magn. Reson. Med. 52, 953–964. doi:10.1002/mrm.20281

Wong, E., 2012. Optimized phase schedules for minimizing peak RF power in simultaneous multi-slice RF excitation pulses. Presented at the Proceedings of the 20th Annual Meeting of ISMRM, Melbourne, Australia, p. 2209.

Wu, X., Schmitter, S., Auerbach, E.J., Uğurbil, K., Van de Moortele, P.-F., 2016. A generalized slab-wise framework for parallel transmit multiband RF pulse design. Magn. Reson. Med. 75, 1444–1456. doi:10.1002/mrm.25689

Wu, X., Vu, A., Schmitter, S., Auerbach, E., Moeller, E., Lenglet, C., Yacoub, E., Van de Moortele, P., Ugurbil, K., 2014. Whole brain single shot diffusion weighted EPI at 7

Tesla using parallel transmit multislice multiband RF pulses. Presented at the Proc. Int. Soc. Mag. Reson. Med, p. 311.

Xu, J., Moeller, S., Auerbach, E.J., Strupp, J., Smith, S.M., Feinberg, D.A., Yacoub, E., Uğurbil, K., 2013. Evaluation of slice accelerations using multiband echo planar imaging at 3 T. NeuroImage 83, 991–1001. doi:10.1016/j.neuroimage.2013.07.055

Yacoub, E., Duong, T.Q., Van De Moortele, P.-F., Lindquist, M., Adriany, G., Kim, S.-G., Uğurbil, K., Hu, X., 2003. Spin-echo fMRI in humans using high spatial resolutions and high magnetic fields. Magn. Reson. Med. 49, 655–664. doi:10.1002/mrm.10433

Yacoub, E., Harel, N., Ugurbil, K., 2008. High-field fMRI unveils orientation columns in humans. Proc. Natl. Acad. Sci. 105, 10607–10612. doi:10.1073/pnas.0804110105

Yacoub, E., Shmuel, A., Logothetis, N., Uğurbil, K., 2007. Robust detection of ocular dominance columns in humans using Hahn Spin Echo BOLD functional MRI at 7 Tesla. NeuroImage 37, 1161–1177. doi:10.1016/j.neuroimage.2007.05.020

Yacoub, E., Shmuel, A., Pfeuffer, J., Van De Moortele, P.-F., Adriany, G., Andersen, P., Vaughan, J.T., Merkle, H., Ugurbil, K., Hu, X., 2001. Imaging brain function in humans at 7 Tesla. Magn. Reson. Med. 45, 588–594. doi:10.1002/mrm.1080

Zhao, F., Wang, P., Hendrich, K., Ugurbil, K., Kim, S.-G., 2006. Cortical layer-dependent BOLD and CBV responses measured by spin-echo and gradient-echo fMRI: Insights into hemodynamic regulation. NeuroImage 30, 1149–1160. doi:10.1016/j.neuroimage.2005.11.013

Zimmermann, J., Goebel, R., De Martino, F., van de Moortele, P.-F., Feinberg, D., Adriany, G., Chaimow, D., Shmuel, A., Uğurbil, K., Yacoub, E., 2011. Mapping the Organization of Axis of Motion Selective Features in Human Area MT Using High-Field fMRI. PLoS ONE 6, e28716. doi:10.1371/journal.pone.0028716

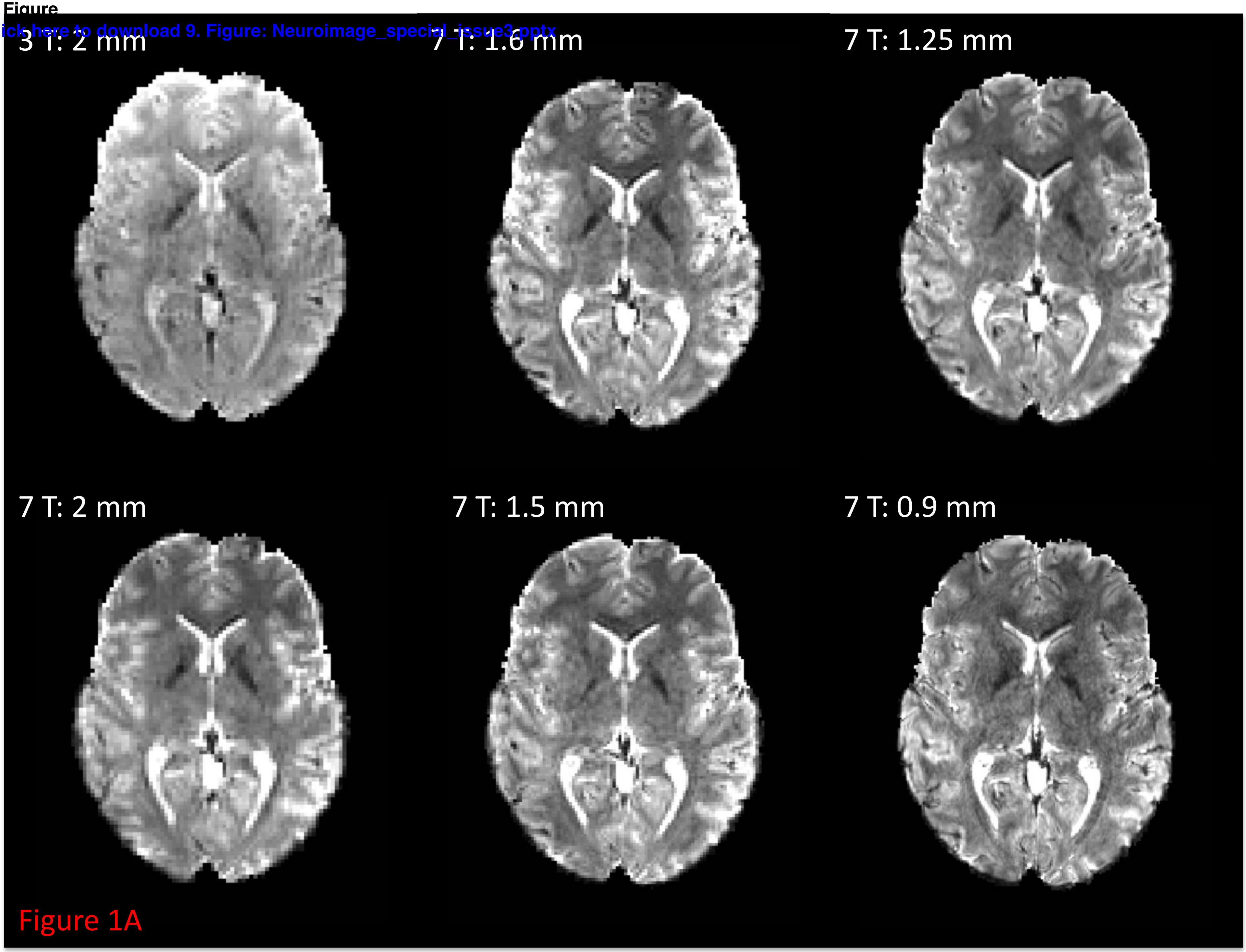

Figure 1A

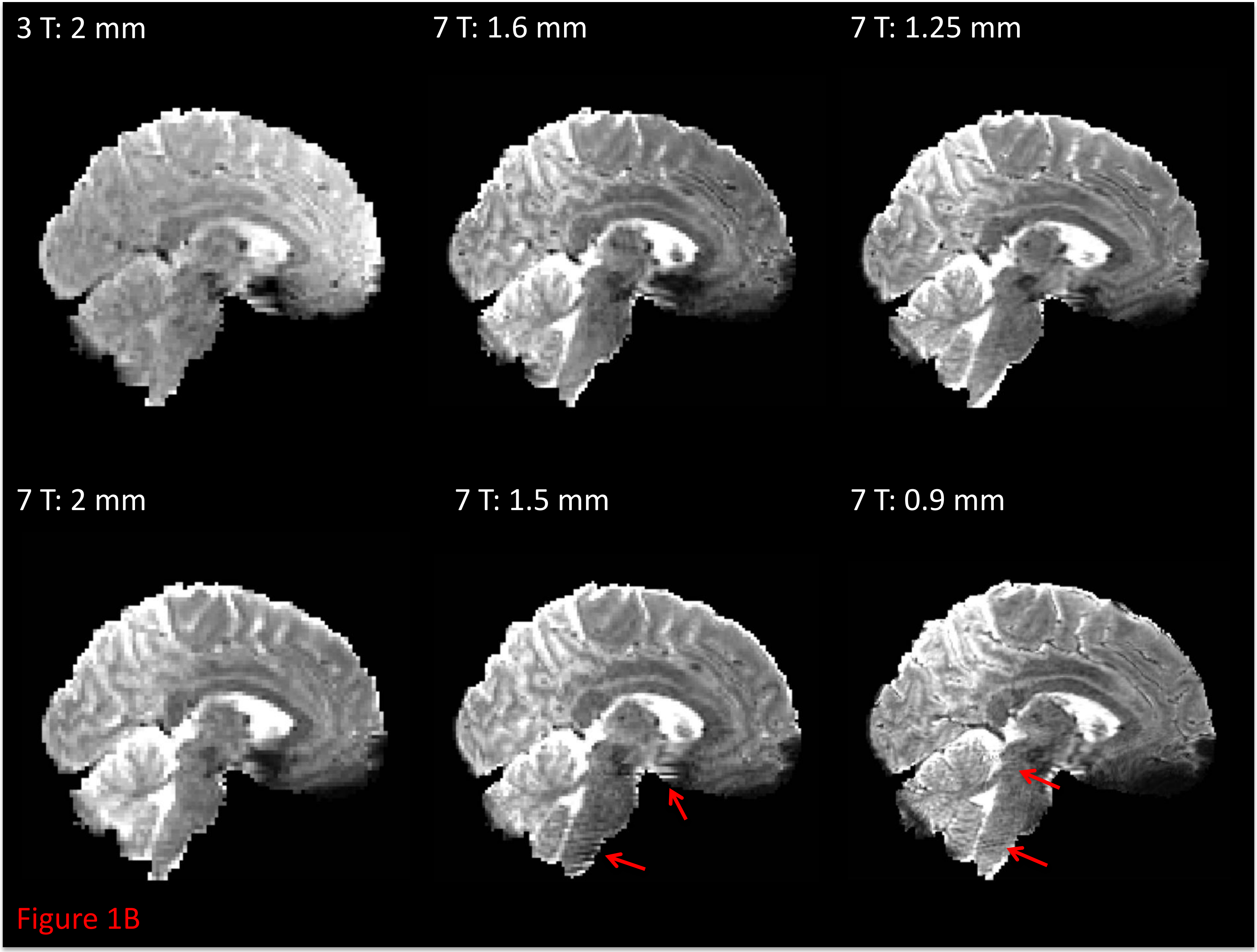

Figure 1B

Figure 2

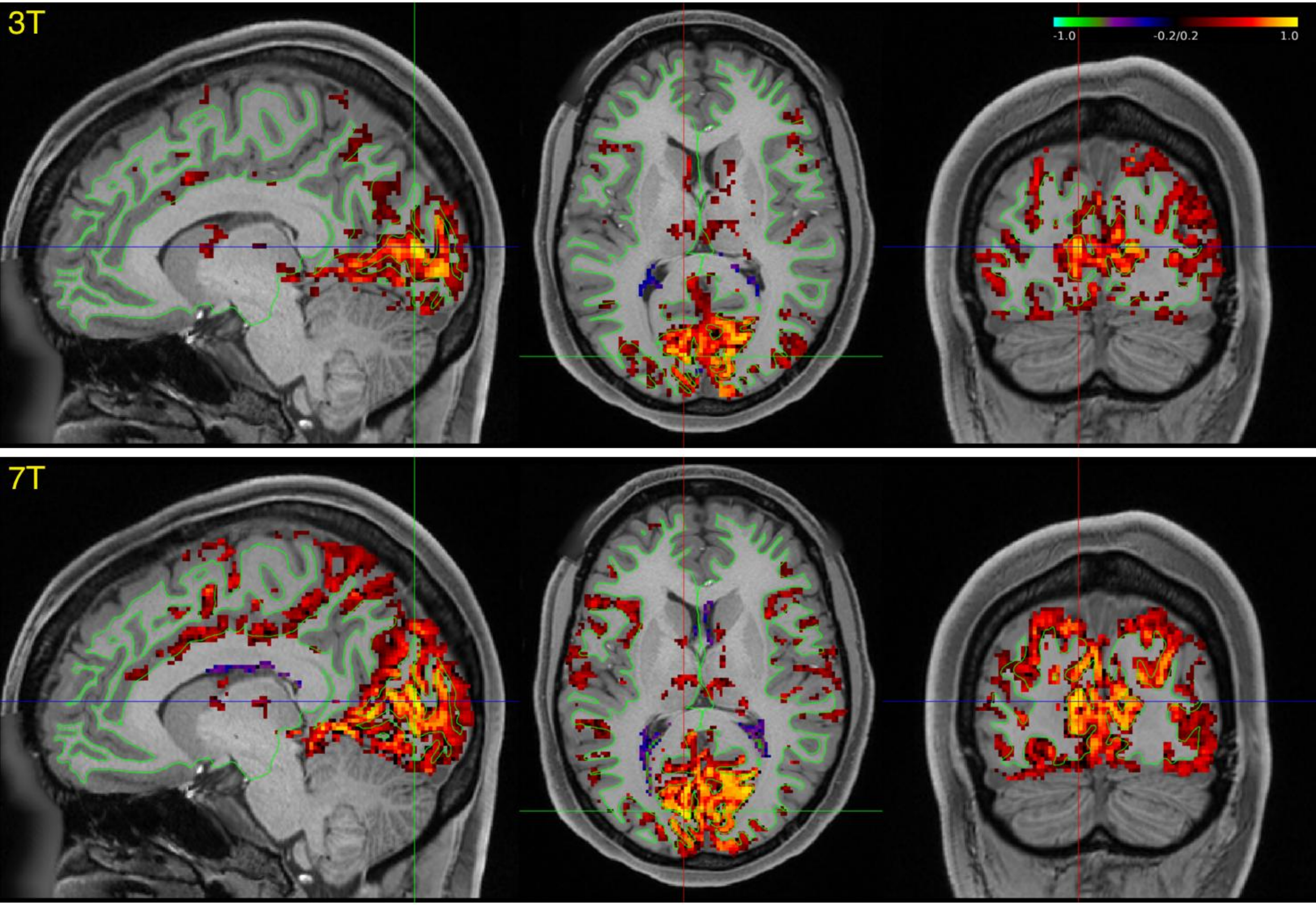

Figure 3

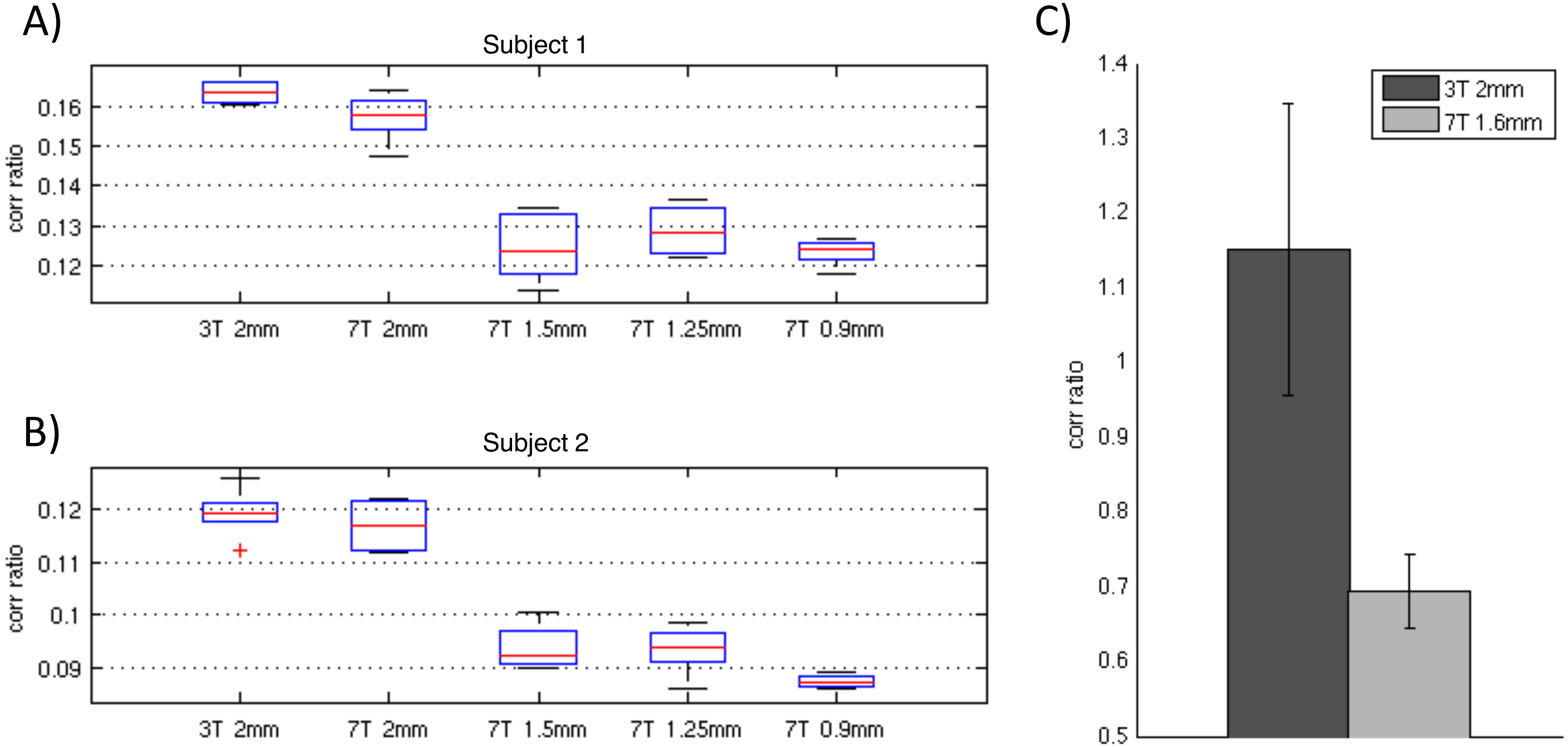
A)
Subject 1
corr ratio
0.16
0.15
0.14
0.13
0.12
3T 2mm
7T 2mm
7T 1.5mm
7T 1.25mm
7T 0.9mm
B)
Subject 2
corr ratio
0.12
0.11
0.1
0.09
3T 2mm
7T 2mm
7T 1.5mm
7T 1.25mm
7T 0.9mm
C)
1.4
1.3
1.2
1.1
1
0.9
0.8
0.7
0.6
0.5
corr ratio
3T 2mm
7T 1.6mm

Figure 4

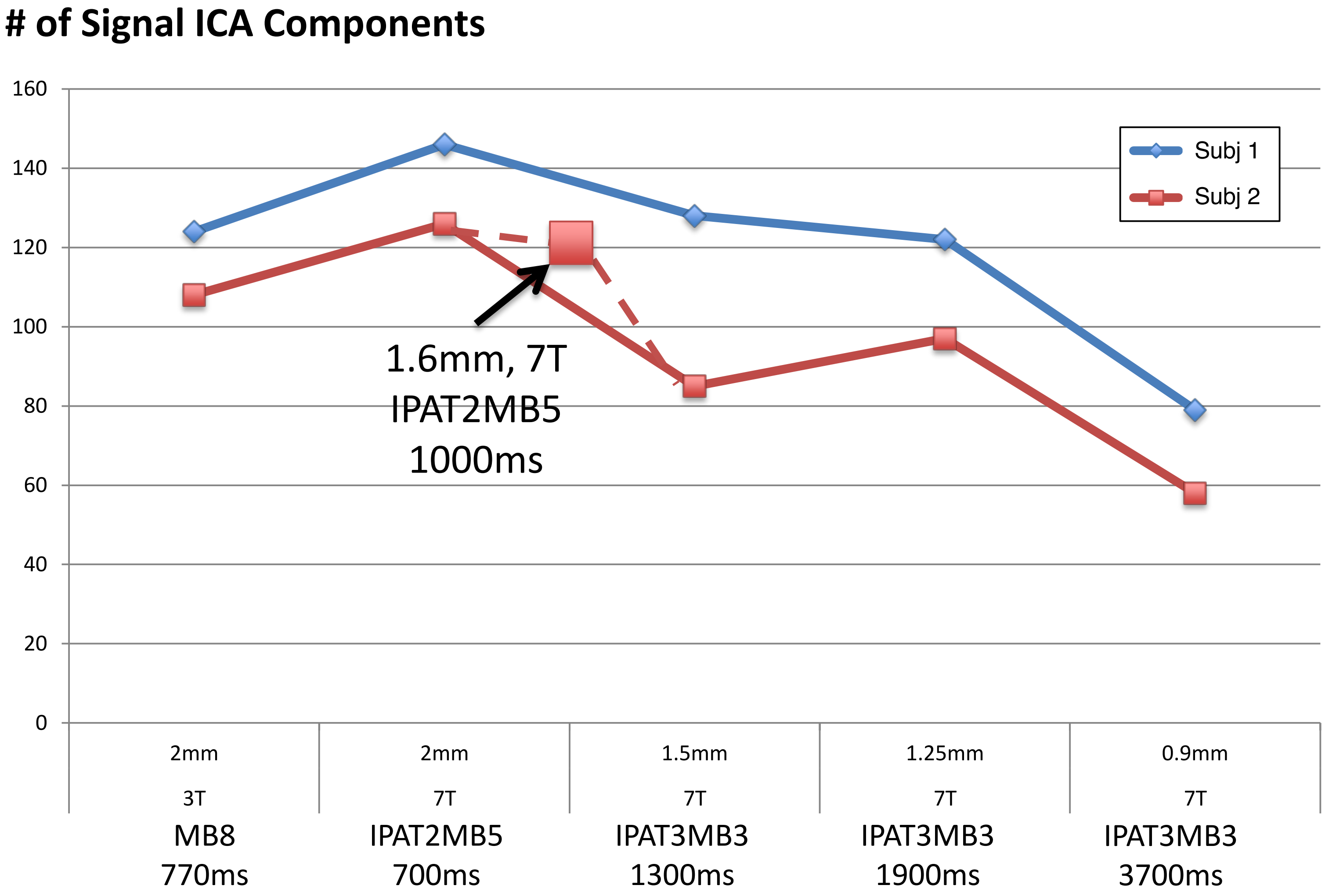

# of Signal ICA Components
160
140
120
100
80
60
40
20
0
Subj 1
Subj 2
1.6mm, 7T
IPAT2MB5
1000ms
2mm
3T
MB8
770ms
2mm
7T
IPAT2MB5
700ms
1.5mm
7T
IPAT3MB3
1300ms
1.25mm
7T
IPAT3MB3
1900ms
0.9mm
7T
IPAT3MB3
3700ms

Figure 5

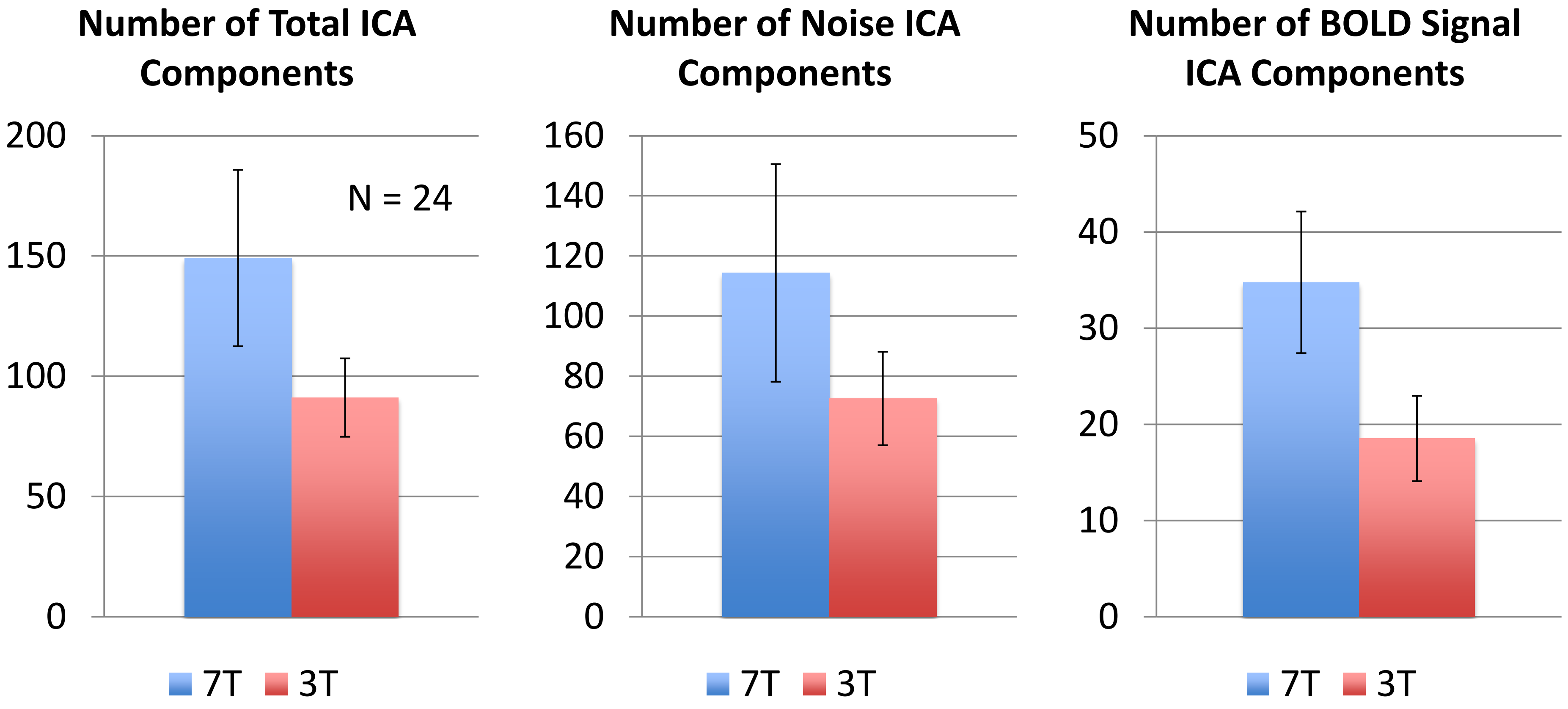

Number of Total ICA Components

Number of Noise ICA Components

Number of BOLD Signal ICA Components

Figure 6

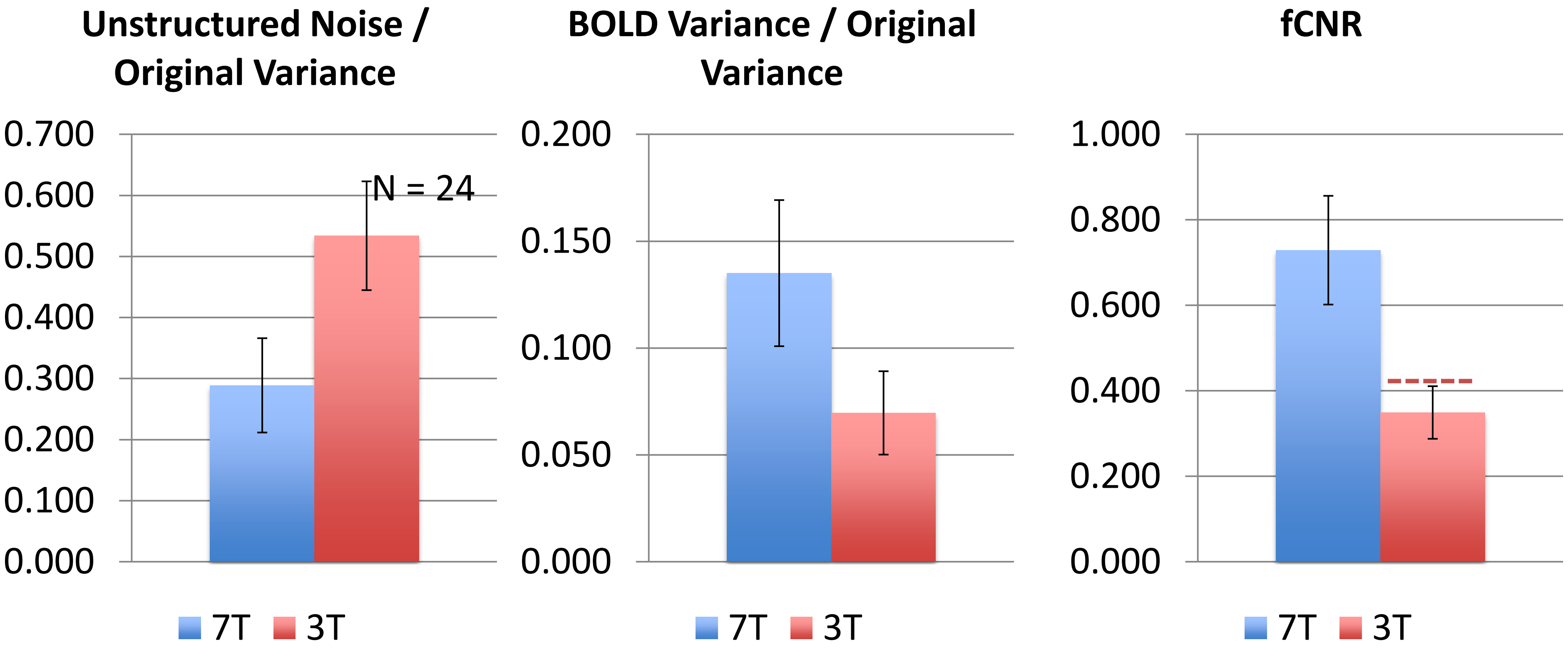
Unstructured Noise / Original Variance
0.700
0.600
0.500
0.400
0.300
0.200
0.100
0.000
N = 24
7T
3T
BOLD Variance / Original Variance
0.200
0.150
0.100
0.050
0.000
7T
3T
fCNR
1.000
0.800
0.600
0.400
0.200
0.000
7T
3T

Figure 7

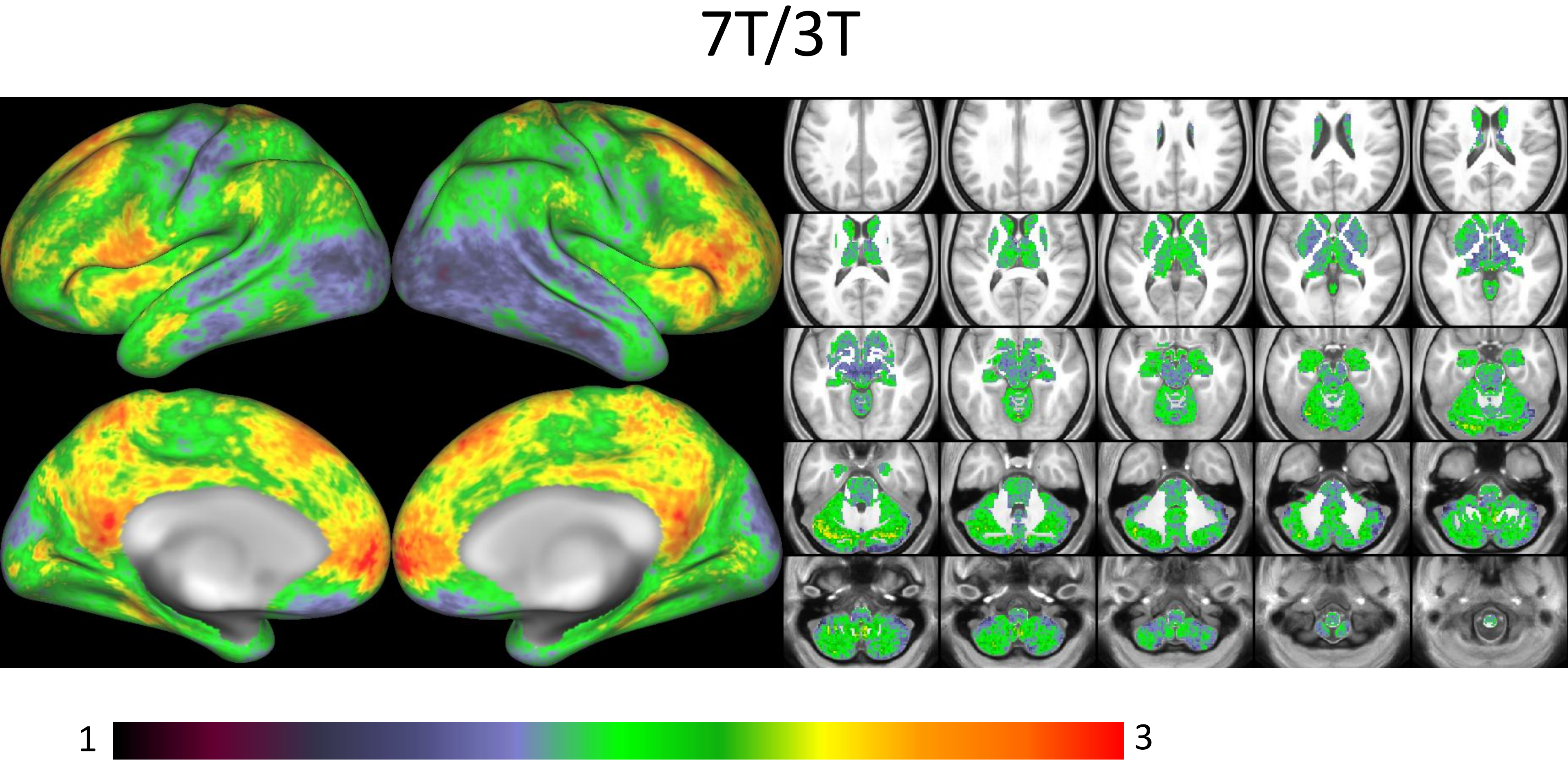

Figure 8

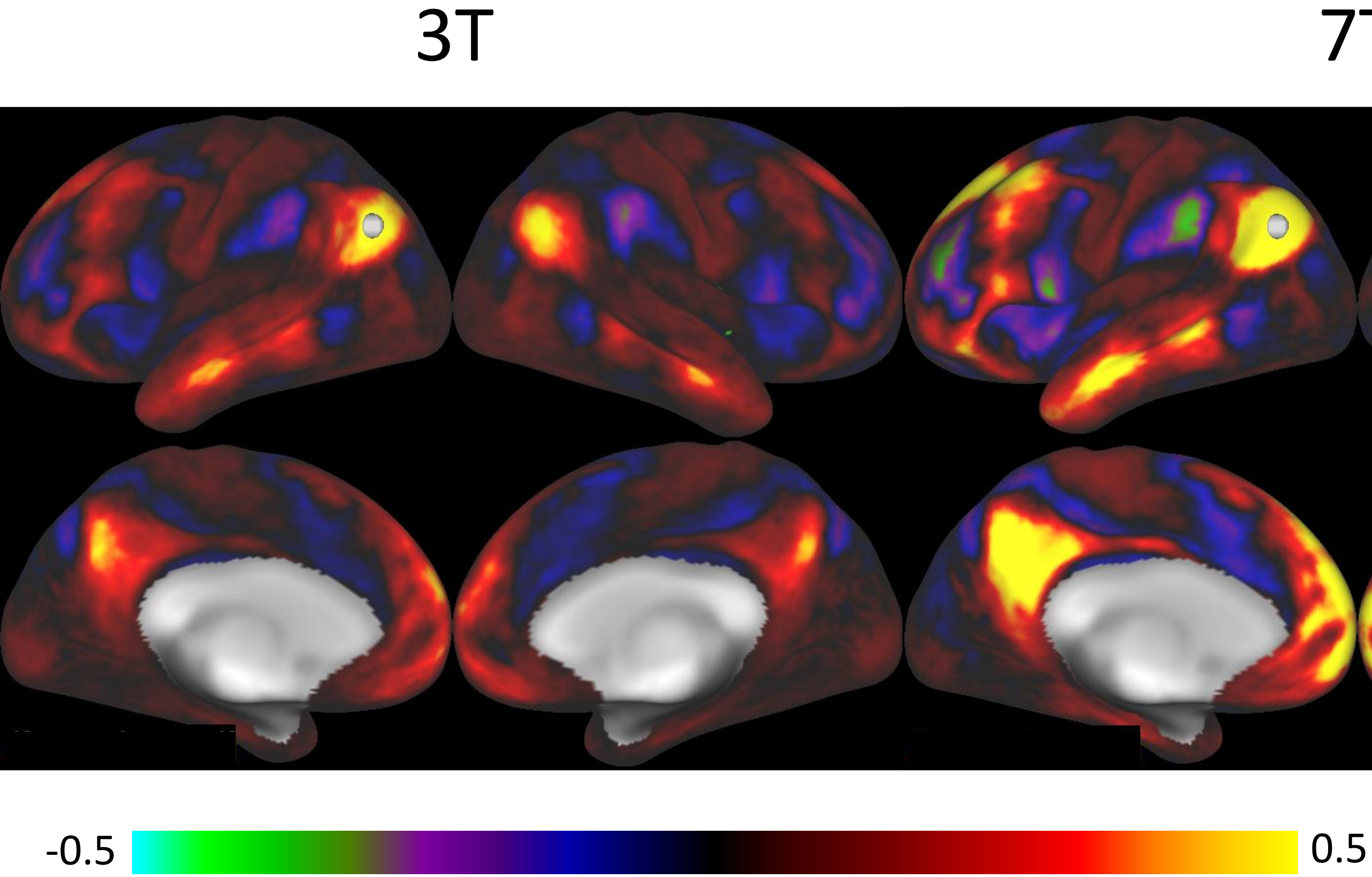

Figure 9

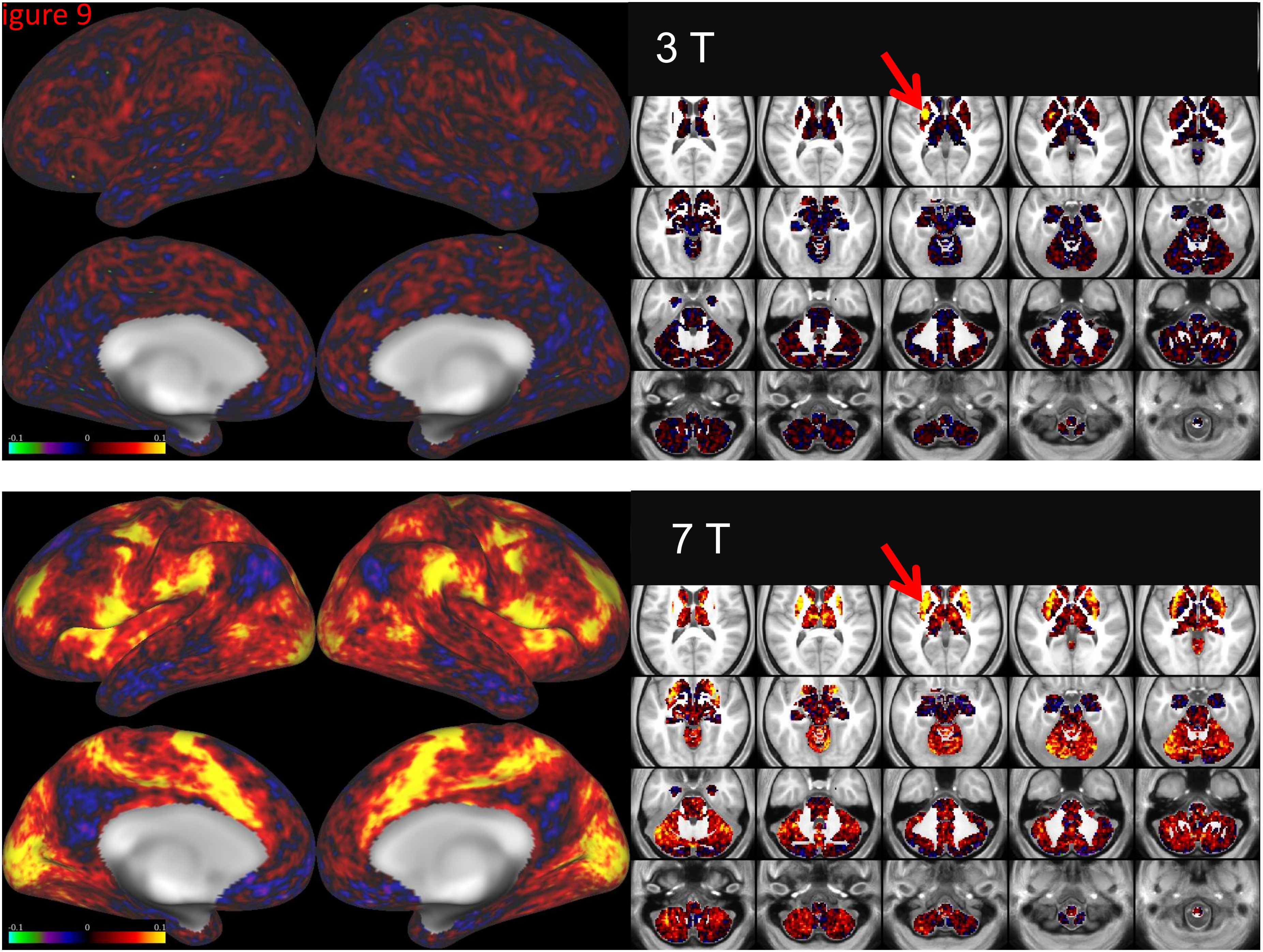

Figure 10